INTERFACE

rsif.royalsocietypublishing.org

Research

Cite this article: Wang S, Zhang X, He G, Liu T. 2015 Lift enhancement by bats' dynamically changing wingspan. *J. R. Soc. Interface* **12**: 20150821.
http://dx.doi.org/10.1098/rsif.2015.0821

Received: 15 September 2015
Accepted: 27 November 2015

Subject Areas:
biomechanics, bioengineering

Keywords:
bat flight, flapping flight, dynamically changing wingspan, unsteady aerodynamics

Author for correspondence:
Guowei He
e-mail: hgw@lnm.imech.ac.cn

Electronic supplementary material is available at http://dx.doi.org/10.1098/rsif.2015.0821 or via http://rsif.royalsocietypublishing.org.

THE ROYAL SOCIETY PUBLISHING

Lift enhancement by bats' dynamically changing wingspan

Shizhao Wang[1], Xing Zhang[1], Guowei He[1] and Tianshu Liu[1,2]

[1]The State Key Laboratory of Nonlinear Mechanics, Institute of Mechanics, Chinese Academy of Sciences, Beijing 100190, People's Republic of China
[2]Department of Mechanical and Aerospace Engineering, Western Michigan University, Kalamazoo, MI 49008, USA

This paper elucidates the aerodynamic role of the dynamically changing wingspan in bat flight. Based on direct numerical simulations of the flow over a slow-flying bat, it is found that the dynamically changing wingspan can significantly enhance the lift. Further, an analysis of flow structures and lift decomposition reveal that the elevated vortex lift associated with the leading-edge vortices intensified by the dynamically changing wingspan considerably contributed to enhancement of the time-averaged lift. The nonlinear interaction between the dynamically changing wing and the vortical structures plays an important role in the lift enhancement of a flying bat in addition to the geometrical effect of changing the lifting-surface area in a flapping cycle. In addition, the dynamically changing wingspan leads to the higher efficiency in terms of generating lift for a given amount of the mechanical energy consumed in flight.

1. Introduction

Biological flapping flight has always inspired human's imagination of flight. However, compared to the remarkable development of modern fixed-wing aircraft, our understanding of flapping flight is still limited due to the complexity of highly unsteady separated flows generated by flapping wings. Low-Reynolds-number flapping flight has recently attracted considerable attention in the aeronautical community due to the need to develop biologically inspired micro air vehicles (MAVs), and some success of building flapping MAVs has been achieved. Study of natural flyers is still a feasible way to improve the flight performance of MAVs, and therefore considerable efforts have been made on the flapping flight of insects, birds and bats [1–11].

Bats are the only flying mammals that are comparable to small birds in terms of the flight characteristics. However, bats have some unique features that are significantly different from birds, including the special skeletal anatomical structure with more degrees of freedom, highly deformable wing-membrane skin and more complicated wing kinematics [12–14]. Bats are more manoeuvrable and capable in slow flight [14–18]. Compared with a large body of literature on the flight of birds and insects, the results on flying bats are relatively limited. The studies of bat flight began from quantitative measurements of bat wing kinematics by using multiple cameras when a trained bat flies in a wind tunnel or a flight cage. Then, the major kinematical quantities of the flapping wing are extracted, including the wingbeat frequency, wingbeat amplitude, stroke plane angle, wing twist, local angle of attack (AoA) and camber. Based on these quantities, the bat wing surface can be reconstructed for experimental and computational analysis. Detailed measurements of the wing kinematics of a lesser dog-faced fruit bat (*Cynopterus brachyotis*) flying a cage were conducted by Tian *et al.* [19], and the trajectories of the wingtip and several digital points and the Strouhal numbers were presented. Further measurements of the wing kinematics of a lesser dog-faced fruit bat were conducted in a wind tunnel by Hubel *et al.* [20,21]. The complex kinematics of the bat wings was reconstructed by Riskin *et al.* [22] using the proper orthogonal decomposition from time-resolved measurements of targets on the wings. The more complete kinematical

data of a Pallas' long-tongued bat (*Glossophaga soricina*) were presented by Wolf *et al.* [23].

To understand the flow structures generated by the bat wings and their relationship with the aerodynamic performance, particle image velocimetry (PIV) measurements synchronized with the wing kinematical measurements have been conducted. Wake velocity fields on the Trefftz plane behind a dog-faced fruit bat were obtained by Tian *et al.* [19], showing the organized tip vortices. Refined PIV measurements in the wake of a Pallas' long-tongued bat were conducted by Hedenstrom *et al.* [24], revealing that a vortex loop was generated by each wing in one cycle and the wake structure was much more complex than that of a flying bird. Further, Hubel *et al.* [20,21] reconstructed the three-dimensional wake structure and estimated the circulation that is responsible for the lift. PIV measurements by Muijres *et al.* [25] at several spanwise sections near the upper wing surface of a slow-flying bat revealed the formation of the leading-edge vortices (LEVs) that significantly increase the lift in slow-flying bats. In general, bats have the distinct aerodynamic performance associated with unique flow structures [14,18,26–28].

In contrast to insects and birds, bats have more than 10 joints on a wing to actively control the complex wing morphology and kinematics. The dynamically changing wingspan is one of the important kinematical aspects in bat flapping flight especially at low speeds. For example, the minimum wingspan of a slow-flying Pallas' long-tongued bat can be as low as about 60% of the maximum one [23]. It is well known that the wingspan (or wing aspect ratio) has a significant effect on the aerodynamic force of a fixed wing by changing the distance between the tip vortices and the induced downwash velocity [29]. In flapping flight where the LEV contributes considerably to lift, it is reported that the finite wingspan could be helpful to stabilize the LEV [30–32]. However, fixed-span flapping wings are considered in most studies on the effects of the aspect ratio, and the effect of the dynamically changing wingspan on lift generation is rarely discussed.

This work focuses on the effect of the dynamically changing wingspan on lift generation of a slow-flying bat. It is noted that the dynamically changing wingspan of bat wings changes not only the wing aspect ratio but also the wing area, which is significantly different from insect wings. This paper is organized as follows. First, the geometrical and kinematical model of a slow-flying bat is reconstructed based on the measurement data provided by Wolf *et al.* [23], and the corresponding bat model with a fixed wingspan is proposed as a reference for comparison. The numerical method and settings are briefly described. Then, the unsteady flow fields for the two models are obtained in direct numerical simulations (DNS) by solving the incompressible Navier–Stokes (NS) equations. The distinct flow structures, particularly the LEVs, are identified and their connection to lift generation is discussed. The results indicate that the dynamically changing wingspan can significantly enhance lift. Furthermore, based on a decomposition of lift into vortex lift and the fluid-acceleration term, it is shown that the elevated vortex lift corresponds to the LEVs intensified by the dynamically changing wingspan. Finally, the conclusions are drawn, indicating that lift enhancement is related to not only the geometrical effect of changing the lifting-surface area but also the nonlinear effect of the altered vortex structures (e.g. the LEVs) by the dynamically changing wingspan.

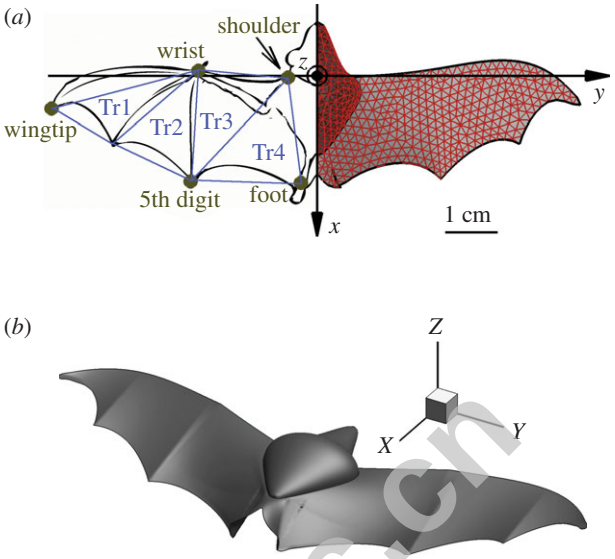

Figure 1. (*a*) The coordinate system and the morphology of the bat wing at the instant when the wingspan reaches the maximum and (*b*) perspective view of the three-dimensional bat model. (Online version in colour.)

2. Geometrical and kinematical models

The morphology and kinematics of two bat models are reconstructed for comparison based on the detailed measurements of slow-flying Pallas' long-tongued bats (*G. soricina*) reported in the work of Wolf *et al.* [23]. The bats had the mean chord length of $c = 3.7$ cm and the weight of 10.7 g. The three-dimensional wingbeat kinematics of the flying bats was extracted from high-speed video taken in a wind tunnel in a range of speeds ($1–7\ \mathrm{m\,s^{-1}}$). Several kinematic and geometric parameters, such as the AoA, span ratio, flapping Strouhal number and downstroke ratio, were determined at different flight speeds. These parameters directly affect the aerodynamic performance of bat flight particularly in lift generation. Wolf *et al.* [23] provided the outline of the wing when the wingspan is at maximum, and the trajectories of the wingtip, wrist, fifth digit, foot and shoulder. These measurement data allow reconstruction of the bat wing geometry and kinematics for numerical simulations. The case with the upstream velocity of $1\ \mathrm{m\,s^{-1}}$ is used in this work.

Figure 1*a* illustrates the coordinate system and the morphology of the wing at the instant when the wingspan reaches maximum. The perspective view of the reconstructed three-dimensional bat model is shown in figure 1*b*. (The projected views of the bat model in the three directions can be found in the electronic supplementary material.) The kinematics of the wingtip, wrist and fifth digit are recovered from the work of Wolf *et al.* [23] and fitted by using the Fourier series while the foot and shoulder are fixed. The trajectories of these key points on the left wing are shown in figure 2. The time-dependent kinematics of these points can be found in the electronic supplementary material. The kinematics of any point on the wing is interpolated from these five key points by using the bi-linear interpolation. The wingspan, defined as the tip-to-tip distance in the spanwise direction, changes with time during flapping flight in this model. The wingspan reaches the maximum $b_{max}/c = 6.0$ in the downstroke and the minimum $b_{min}/c = 3.8$ in the upstroke. The time-averaged wingspan in a flapping period is $b_{mean}/c = 4.4$. For convenience, the simulation based on this model is referred to as the dynamically changing wingspan case.

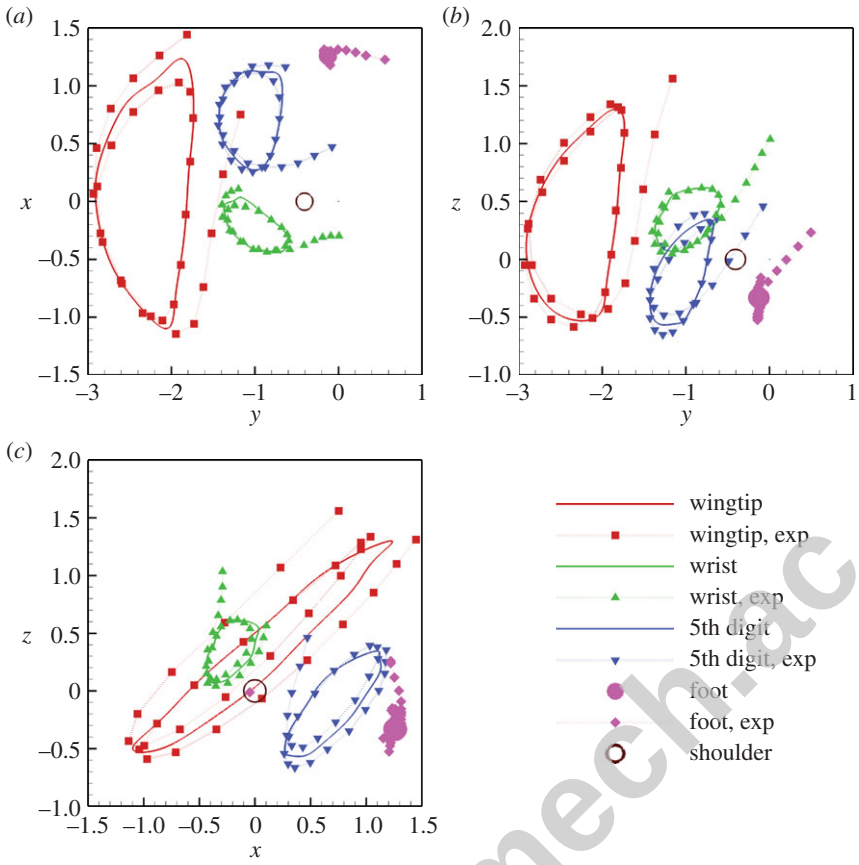

Figure 2. The trajectories of the wingtip, wrist, fifth digit, foot and shoulder used in the present work in comparison with those provided in the measurements of Wolf *et al.* [23] in (*a*) $x-y$ plane, (*b*) $z-y$ plane, (*c*) $z-x$ plane. (Online version in colour.)

To investigate the effect of changing wingspan on lift generation, a hypothetical bat model is considered, in which the streamwise and vertical motions remain the same as those of the first model, but the spanwise motion is turned off. The spanwise positions of the wingtip, wrist and fifth digit are fixed at their time-averaged values, and the fixed wingspan is $b/c = 4.4$. The time-dependent kinematics of these key points can also be found in the electronic supplementary material. This model serves as a reference to identify the effect of dynamically changing wingspan. For convenience, the simulation based on this hypothetical model is referred to as the fixed wingspan case.

To compute the local AoA, the four triangular panels of the left wing are defined as shown in figure 1*a*. The same triangular panels are taken as those given by Wolf *et al.* [23]. The local AoA of each triangular panel is computed as the angle between the panel surface and the velocity vector at its centroid. The time histories of the AoAs in the dynamically changing wingspan case are shown in figure 3*a*, where the measurement results provided by Wolf *et al.* [23] are also plotted for comparison. The time-dependent AoAs described the model with the dynamically changing wingspan are consistent with the measurements in the downstroke ($t = 0.1–0.6$), which also capture the main behaviour in the upstroke ($t = 0.6–1.1$). Figure 3*b* shows the comparisons of the time histories of the AoAs of the four triangular panels between the dynamically changing wingspan case and the fixed wingspan case. The time histories of the AoAs of the panels are essentially the same in both the cases particularly in the downstroke. Therefore, the fixed wingspan model disables the effect of the changing wingspan for a reference without altering the other geometric and kinematic characteristics.

3. Numerical method and settings

The flows around the bat models are governed by the incompressible NS equations and the continuity equation,

$$\frac{\partial \mathbf{u}}{\partial t} + \mathbf{u} \cdot \nabla \mathbf{u} = -\nabla p + \frac{1}{Re}\nabla^2 \mathbf{u} + \mathbf{f}, \tag{3.1}$$

$$\nabla \cdot \mathbf{u} = 0, \tag{3.2}$$

where $\boldsymbol{u}$ and p are the non-dimensional velocity and pressure, respectively, $\boldsymbol{f}$ is a volume force to represent the effect of boundaries on the flows, $Re = U_\infty c/\nu$ is the Reynolds number, υ is the kinematic viscosity and U_∞ is the uniform upstream velocity. The non-dimensional vorticity is defined by $\boldsymbol{\omega} = \nabla \times \mathbf{u}$.

Equations (3.1) and (3.2) are solved numerically by using an immersed boundary method based on the discrete stream function formulation developed by Wang & Zhang [33]. In this method, the NS equations are solved on an Eulerian grid, and the morphology and kinematics of the bat models are described by using Lagrangian points. The effect of the bat surface on flows is represented by the volume forces in the momentum equations. The volume forces are determined by solving a linear equation on Lagrangian points to ensure the non-slip boundary condition on the surface of models. The information on the Eulerian grid and Lagrangian points is interpolated to each other by using a discrete delta function provided by Yang *et al.* [34] to remove the unphysical oscillations. Details of the method can be found in our previous work [33,35].

The computational domain is $[-12c, 20c] \times [-16c, 16c] \times [-24c, 24c]$ in the streamwise (x), spanwise (y) and vertical (z) directions. The unstructured Cartesian grid with hanging-nodes is used to refine the mesh around the body.

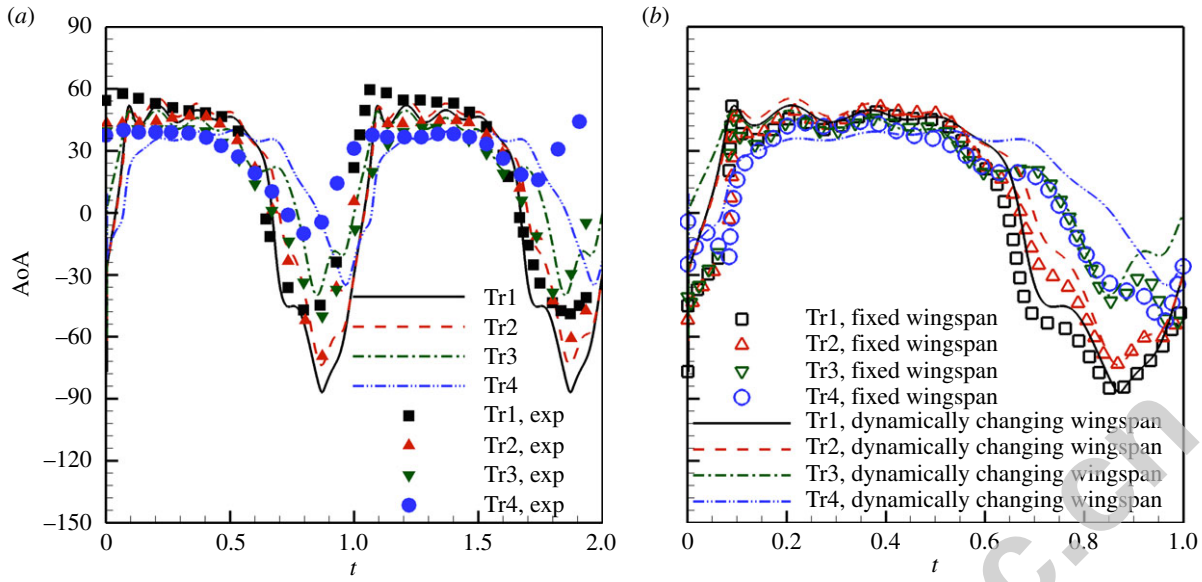

Figure 3. The time histories of the AoA (in degrees) for the four triangular panels: (*a*) comparison between the model with the dynamically changing wingspan and the measurements by Wolf *et al.* [23], and (*b*) comparison between the dynamically changing wingspan case and the fixed wingspan case. (Online version in colour.)

The minimum grid size is $dh/c = 0.02$, and the maximum grid size is $dh/c = 0.32$, where dh is the grid size and c is the base chord. The total number of discretized unstructured cells is 5 369 050. The number of the Lagrangian points on the bat surface is 23 266. The time step is selected to keep the maximum Courant–Friedrichs–Lewy number at 0.5. The independence of the lift coefficient on the grid resolution and computational domain has been examined (see the electronic supplementary material for details). The validations of the method for various flows can be found in our previous work [33,35,36].

The uniform upstream flow is set at the inlet, and the free convection flow at the outlet. The non-slip boundary condition is specified at the surface of the bat models. The zero-shear slip wall conditions are used at other boundaries. The initial condition for the incoming velocity is (1, 0, 0), where the velocity components are normalized by the freestream velocity U_∞. The Strouhal number is $St = fc/U_\infty = 1.36$, which is the same as that in the measurements [23], where f is the flapping frequency. The Reynolds number is fixed at $Re = U_\infty c/v = 300$ which is lower than $Re = 2371$ in the measurements. This lower Reynolds number in DNS is selected to ensure the spatial resolution of the resolved flow field around the bat models. The underlying assumption behind this selection of a lower Reynolds number is that the lift and flow structures of a flapping wing is not very sensitive to the viscosity in this Reynolds number range, which is supported by some studies [28,37–40]. The Reynolds number may affect the separation position of a flow over a blunt body. However, the flow separation over the present bat models is not significantly affected by the Reynolds number since the flow separation always occurs at the sharp leading edges at large AoAs. The limited effects of Reynolds numbers on the aerodynamic forces and vortical structures in flows over flapping wings with sharp leading edges have been found in the studies of climbing bats [28] and other flapping wing models [37–40].

4. Flow structures and lift coefficient

Figure 4 is an overall top view of the streamlines and vortical structures on the upper wing surface of the bat during the downstroke in the dynamic changing wingspan case, where the vortical structures are identified by using the λ_2-criterion [41] and coloured by the normalized spanwise vorticity. The value λ_2 is the second eigenvalue of $\boldsymbol{S}^2 + \boldsymbol{\Omega}^2$, where $\boldsymbol{S}$ and $\boldsymbol{\Omega}$ are the symmetric and antisymmetric components of the velocity gradient tensor, respectively. The most distinct structures are the LEVs generated in the downstroke. The LEVs are bent towards the freestream direction at the wingtips and merged into the wingtip vortices. The LEVs are apparently stabilized along the leading edge in the downstroke. The strength of the LEV increases towards the wingtip. The LEV is an important constituent of an unsteady lift-generating mechanism in bat flight, which will be discussed later based on lift decomposition. The overall flow structures obtained in DNS are consistent with the experimental observations by Hedenstrom *et al.* [24] and Muijres *et al.* [25].

The LEVs are dominated by the spanwise vorticity. The evolution of the vortical structures is visualized by the isosurfaces of the spanwise vorticity at sequential moments in the dynamically changing wingspan case in the upper row of figure 5. It is found that the LEVs are generated at the beginning of the downstroke, which are intensified as the wing moves downward, and shed at the end of the downstroke. The shedding LEVs stays near the upper surface of the wing in the early stage of the upstroke, as shown in the upper row of figure 5*d*. They still contribute to a positive vortex lift even in the upstroke, as shown in §5. This phenomenon is similar to the vortex capture observed by Wang *et al.* [42] on a flapping rectangular morphing wing. For comparison, the corresponding evolution of the LEVs in the fixed wingspan case is shown in the lower row of figure 5. The generation and shedding of the LEVs in the fixed wingspan case are similar to these in the dynamically changing wingspan case. However, the LEVs in the fixed wingspan case are weaker. Since the LEVs correspond to vortex lift generation, the weaker LEVs in the fixed wingspan case will cause smaller vortex lift generation. This will be quantitatively examined based on the lift decomposition in next section. The lift enhancement by the intensified LEVs due to the dynamically changing wingspan is consistent with the results reported by Wang *et al.* [42] on a flapping rectangular morphing wing.

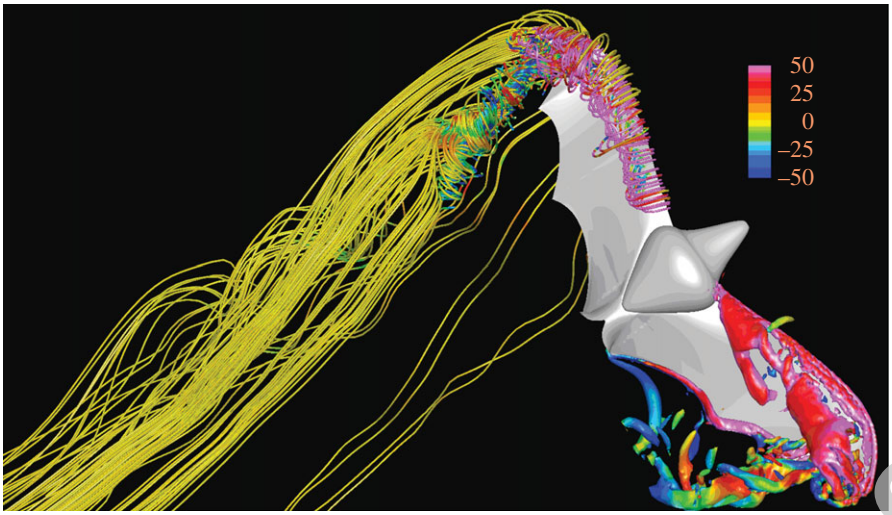

Figure 4. The streamlines and vortical structures around the bat wings when the wingspan reaches the maximum in the dynamically changing wingspan case. The flow structures are identified by using the λ_2-criterion with $\lambda_2 = -500$. The colour indicates the value of the normalized spanwise vorticity.

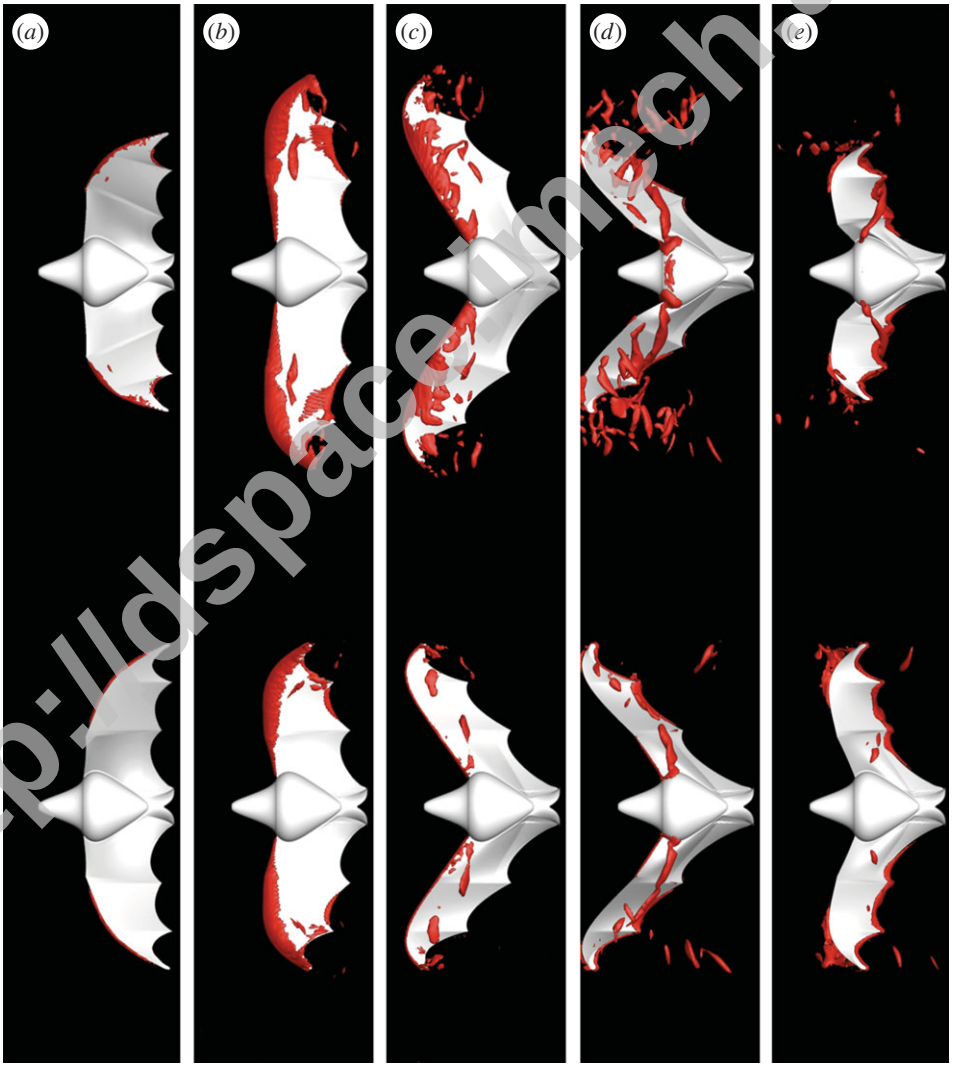

Figure 5. The iso-surfaces of the spanwise vorticity on the upper wing surface in the dynamically changing wingspan case (upper row) and the fixed wingspan case (lower row) at (*a*) the beginning of the downstroke, (*b*) the middle of the downstroke, (*c*) the end of the downstroke, (*d*) the early stage of the upstroke (0.1 T after the start of the upstroke) and (*e*) the middle of upstroke. The iso-surfaces of $\omega_y = 100$ are plotted in (*a*–*c*). The iso-surfaces of $\omega_y = 50$ are plotted in (*d*,*e*).

Figure 6 shows the time histories of the lift coefficient $\mathrm{Cl}(t) = L(t)/q_\infty S_{\mathrm{avg}}$ in one flapping period for the dynamically changing wingspan case and the fixed wingspan case, where $L(t)$ is the lift, $q_\infty = \rho U_\infty^2/2$ is the dynamic pressure, S_{avg} is the averaged wing area. It is shown in figure 6 that in both the cases the positive lift is generated in the downstroke and the certain phases of the upstroke, and the negative lift is generated in the mid-span of the upstroke.

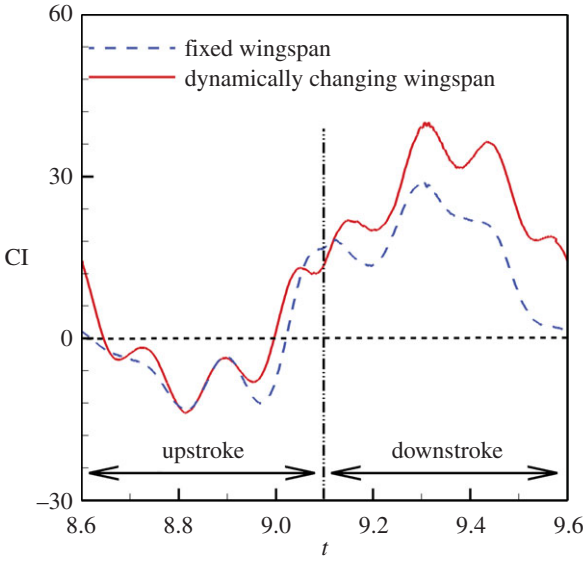

Figure 6. The time histories of the lift coefficient: comparison between the two models of the Pallas' long-tongued bat (*G. soricina*). (Online version in colour.)

The lift coefficient increases from about 2/5 of the upstroke at which the lift coefficient has a negative peak. The positive peak of the lift coefficient is attained at the middle of the downstroke. The lift coefficient remains positive during the transition stage from the downstroke to the upstroke, which is attributed to the positive vortex lift in the upstroke (see §5). The time history of the lift coefficient for the Pallas' long-tongued bat is similar to that reported by Wang *et al.* [43] for a model of the grey-headed flying fox (*Pteropus poliocephalus*) with different wing morphology at a higher Reynolds number (1000). However, there are some differences in the detailed histories of the lift coefficient between the two kinds of bats, which might be associated with the different wing geometry. A comparison of the lift coefficients between bat models with different wing morphologies is given in the electronic supplementary material. A detailed comparative study will be presented in a separate paper.

The lift coefficient in the dynamically changing wingspan case is denoted by the solid line in figure 6, and the time-averaged lift coefficient in one flapping period is $\langle \mathrm{Cl} \rangle_T \approx 12.6$, where $\langle \bullet \rangle_T = T^{-1} \int_0^T \bullet \mathrm{d}t$ is the time-averaging operator in a flapping period T. The dashed line in figure 6 shows the lift coefficient in the fixed wingspan case for comparison. The increment $\Delta\langle \mathrm{Cl} \rangle_T = \langle \mathrm{Cl} \rangle_T - \langle \mathrm{Cl} \rangle_{T,\mathrm{ref}}$ represents the effect of the dynamically changing wingspan on the lift coefficient, where $\langle \mathrm{Cl} \rangle_{T,\mathrm{ref}}$ is the time-averaged lift coefficient in the fixed wingspan case as a reference. The time-averaged lift coefficient in the fixed wingspan case is $\langle \mathrm{Cl} \rangle_{T,\mathrm{ref}} \approx 6.6$. The increment $\Delta\langle \mathrm{Cl} \rangle_T \approx 6$ is about 91% of the lift coefficient $\langle \mathrm{Cl} \rangle_{T,\mathrm{ref}}$ in the fixed wingspan case. This indicates that the lift is significantly enhanced by the dynamically changing wingspan of a flying bat.

Two mechanisms contribute to lift enhancement: the geometrical effect of the dynamically changing lifting-surface area in a flapping cycle and the fluid-mechanic effect of the altered vortical structures induced by the dynamically changing wingspan. It is clear that the changing wing area in a flapping cycle would affect the time-averaged lift. Generally, the wingspan stretches outward during the downstroke and retracts inward to the body during the upstroke. For a flapping wing with the time-dependent wing area $S(t)$, the time-averaged lift is $\langle L \rangle_T = q_\infty \langle \mathrm{Cl}_s(t) S(t) \rangle_T$, where $\mathrm{Cl}_s(t) = L(t)/q_\infty S(t)$ is the lift coefficient defined based on the instantaneous wing area $S(t)$. In the limiting case where $\langle \mathrm{Cl}_s \rangle_T = 0$, the positive time-averaged lift ($\langle L \rangle_T > 0$) could be still generated as the pure geometrical effect associated with the dynamically changing wing area as long as the positive correlation $\langle \mathrm{Cl}_s(t) S(t) \rangle_T > 0$ is achieved. Since the instantaneous lift coefficient $Cl_s(t)$ largely eliminates the geometrical effect, the time-averaged lift coefficient $\langle \mathrm{Cl}_s \rangle$ represents the lift generated by the altered vortical structures by the dynamic changing wingspan.

Accordingly, the increment $\Delta\langle \mathrm{Cl}_s \rangle_T = \langle \mathrm{Cl}_s \rangle_T - \langle \mathrm{Cl}_s \rangle_{T,\mathrm{ref}}$ represents the effect of the dynamically changing wingspan on the lift coefficient after the geometrical effect is removed, which is a result of nonlinear interaction between the wing and vortex structures. The increment of the lift coefficient based on the instantaneous wing area is $\Delta\langle \mathrm{Cl}_s \rangle_T \approx 3.2$, which is about 53% of the total increment of $\Delta\langle \mathrm{Cl} \rangle_T \approx 6$. This means that the lift enhancement is not only caused by the geometrical effect of changing wing area but also the fluid-mechanic effect of the altered vortex structures associated with the dynamically changing wingspan. To illustrate this point, the distributions of the spanwise vorticity on the wing in the dynamically changing wingspan case and the fixed wingspan case at the end of the downstroke are shown in figure 7. The strong shear layer generated at the leading edge rolls into the LEVs that grow in size while travelling downstream on the upper surface in both the cases. It is clearly observed that the LEVs generated in the dynamically changing wingspan case (figure 7*a*) are much stronger than that in the fixed wingspan case (figure 7*b*). This is also evidenced by the distributions of the spanwise vorticity in the spanwise slices at 60% semi-wingspan in figure 7*c*,*d*. The magnitude of the positive spanwise vorticity on the upper surface of the wing in the dynamically changing wingspan case (figure 7*c*) is much higher than that in the fixed wingspan case (figure 7*d*). This phenomenon corresponds to lift enhancement. Figure 8 shows the distributions of the normalized spanwise vorticity at the end of the downstroke at the spanwise locations of 20, 40, 60 and 80% semi-wingspan. The larger magnitudes of the positive spanwise vorticity on the upper wing surface are found at these locations in the dynamically changing wingspan case.

It is noted that the absolute time-average lift calculated at the flight speed of 1 m s^{-1} in this work is about half of the weight (10.7 g) of the slow-flying Pallas' long-tongued bat measured in the experiments of Wolf *et al.* [23]. There are some possible reasons for underestimating the time-averaged lift. The present bat model is reconstructed based on the measurement data of the five key points (joints) on the wing (wingtip, wrist, fifth digit, foot and shoulder). Although this model captures the main kinematical features, the complex surface geometry between these joints is not considered. There is the passive and actively controlled deformation of the flexible muscularized membranes of a bat wing, which is characterized by the wing cambering, bending and twisting. This deformation could play an important role in lift generation and propulsion [27,28]. In the future work, the more detailed geometry and kinematics of the deformable surface should be incorporated into an improved bat model. Since the lift enhancement related to the dynamically changing wingspan is the focus of this work, it is reasonable to use the lift coefficient as a relative comparative measure even though the calculated absolute lift is not enough to support the weight of the bat.

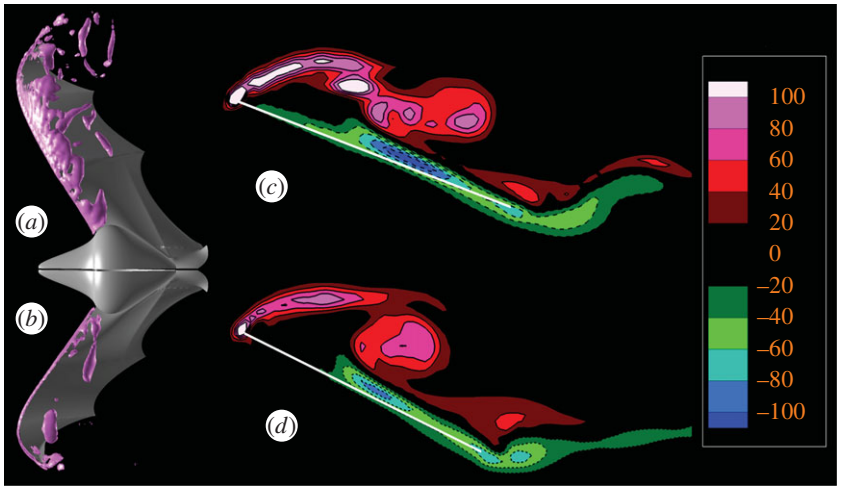

Figure 7. The distributions of the normalized spanwise vorticity around the bat wings at the end of the downstroke. Panels (*a*,*b*) are the top views of the iso-surface of $\omega_y = 100$ on the right wing in the dynamically changing wingspan case and on the left wing in the fixed wingspan case, respectively. Panels (*c*,*d*) show the distributions of the normalized spanwise vorticity in the slices at 60% of the semi-wingspan from the body in the dynamically changing wingspan case and the fixed wingspan case, respectively.

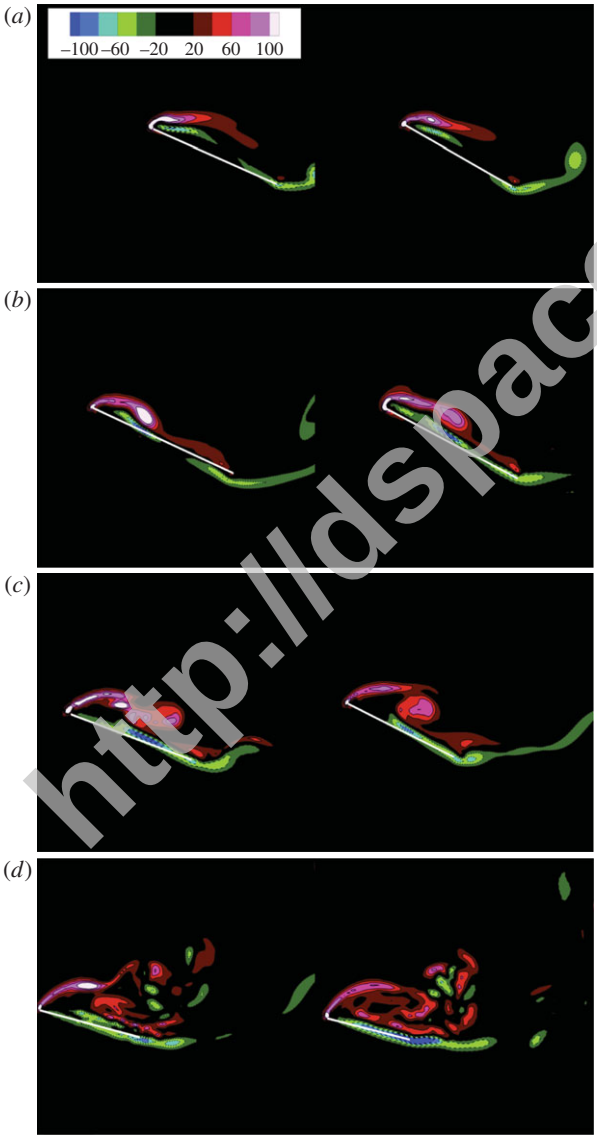

Figure 8. The distributions of the normalized spanwise vorticity at the end of the downstroke at the spanwise locations of (*a*) 20, (*b*) 40, (*c*) 60 and (*d*) 80% semi-wingspan. The left column shows the dynamically changing wingspan case, and the right column shows the fixed wingspan case.

An interesting finding by Lentink & Dickinson [44,45] is that the positional rotational accelerations of an insect wing could stabilize the LEV. The rotational accelerations of the wings as a possible kinematic mechanism could also have effects on the LEVs and their induced lift enhancement in bat flight. Different from an insect wing, the bat wing should be modelled by a multiple-body system [8,46,47]. The rotational accelerations can be adopted for the different segments based on the original definitions given in reference [44]. However, detailed studies are required in the future to clarify the quantitative connection between the rotational accelerations and the lift enhancement in bat flight.

5. Lift decomposition

Further, the relationship between lift generation and vortical structures is explored based on the lift decomposition into the vortex force and the fluid acceleration term. For a columnar control volume whose upper and lower faces are sufficiently far away from a wing and the vertical faces enclose all vortical structures between the leading and trailing edges of the wing, the simple lift formula for forward flight is given in the two dominant terms [36,48], i.e.

$$L \approx L_{\mathrm{vor}} + L_{\mathrm{acc}}. \tag{5.1}$$

The vortex lift is

$$L_{\mathrm{vor}} = \rho \boldsymbol{k} \cdot \int_{V_{\mathrm{f}}} \mathbf{u} \times \boldsymbol{\omega}\, \mathrm{d}V \tag{5.2}$$

and the lift associated with the fluid acceleration is

$$L_{\mathrm{acc}} = -\rho \boldsymbol{k} \cdot \int_{V_{\mathrm{f}}} \frac{\partial \mathbf{u}}{\partial t} \mathrm{d}V - \rho \boldsymbol{k} \cdot \oint_{\partial B} \left(\frac{|\boldsymbol{u}|^2}{2} \right) \mathbf{n}\, \mathrm{d}S, \tag{5.3}$$

where $\boldsymbol{u}$ is the velocity, $\boldsymbol{\omega}$ is the vorticity, V_{f} denotes the columnar control volume of fluid, ∂B denotes the boundary of the wing domain, $\boldsymbol{k}$ is the unit vector normal to the free-stream velocity and $\boldsymbol{n}$ is the unit normal vector pointing to the inside of the wing body. The volume integral of the Lamb vector $\boldsymbol{u} \times \boldsymbol{\omega}$ in equation (5.2) represents the vortex

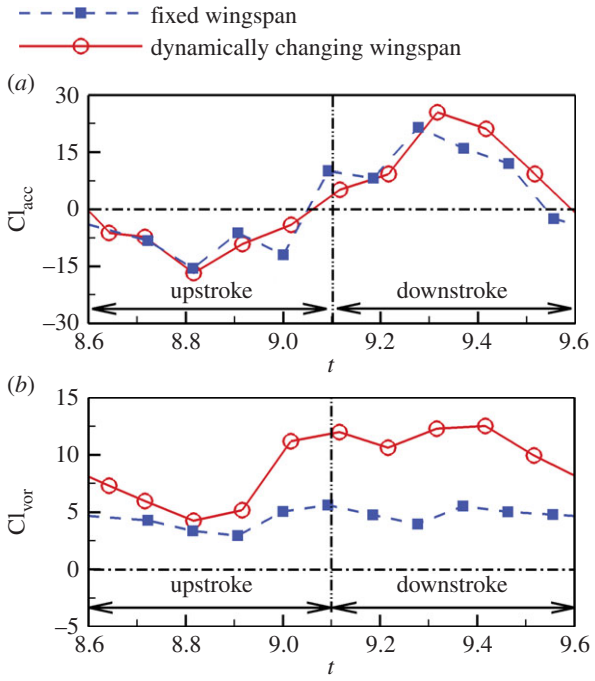

Figure 9. The decomposition of the lift acting on the bat models into (*a*) the fluid acceleration term and (*b*) the vortex lift. (Online version in colour.)

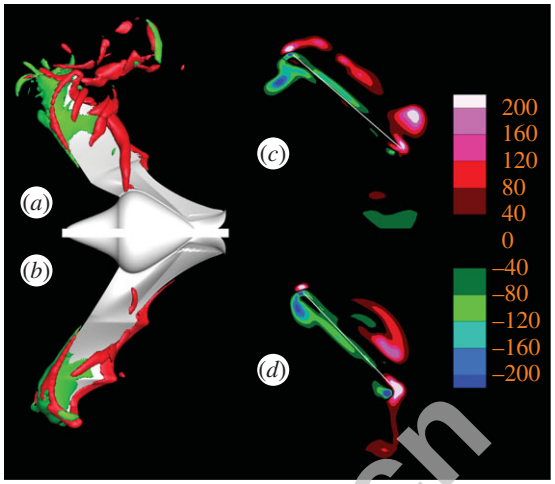

Figure 10. The distributions of the vertical component of the Lamb vector around the bat wings at 0.2 T after the start of the upstroke. Panels (*a*) and (*b*) are the top views of the iso-surface of $(\boldsymbol{u} \times \boldsymbol{\omega})_z = \pm 100$ on the right wing in the dynamically changing wingspan case and on the left wing in the fixed wingspan case, respectively. Panels (*c*) and (*d*) show the distributions of the vertical component of the Lamb vector in the slices at 60% of the semi-wingspan from the body in the dynamically changing wingspan case and the fixed wingspan case, respectively.

force. In a special case where the flow becomes inviscid and irrotational, L_{acc} is reduced to added-mass lift. The accuracy of the simple lift formula applied to several unsteady flows has been validated by Wang *et al.* [36], and the validation of this lift formula in this present case can be found in the electronic supplementary material. In the case where the bat wing membrane is treated as an infinitely thin layer, the second integral on the right-hand side of equation (5.2) is zero.

The coefficients of the vortex lift and the lift associated with fluid acceleration are defined as $Cl_{vor} = L_{vor}/q_\infty S_{avg}$ and $Cl_{acc} = L_{acc}/q_\infty S_{avg}$, respectively. The time histories of Cl_{vor} and Cl_{acc} in one flapping period are shown in figure 9 for both the dynamically changing wingspan case and fixed wingspan case. The lift coefficient associated with the fluid acceleration (Cl_{acc}) varies from −16.5 in the upstroke to 25.3 in the downstroke in the dynamically changing wingspan case. The corresponding variation in the fixed wingspan case is from −15.5 in the upstroke to 19.6 in the downstroke. This lift coefficient associated with fluid acceleration dominates the temporal variation in the lift coefficient Cl. However, the time-average lift coefficient associated with the fluid acceleration ($\langle Cl_{acc}\rangle_T$) is not the main contributor to the time-averaged lift coefficient $\langle Cl\rangle_T$. The time-averaged contributions are $\langle Cl_{acc}\rangle_T \approx 3.1$ in the dynamically changing wingspan case and $\langle Cl_{acc}\rangle_T \approx 1.8$ in the fixed wingspan case, which are about 25% and 27% of $\langle Cl\rangle_T$, respectively. In contrast, the time-averaged vortex lift coefficients of the flying bat are $\langle Cl_{vor}\rangle_T \approx 9.5$ in the dynamically changing wingspan case and $\langle Cl_{vor}\rangle_T \approx 4.8$ in the fixed wingspan case, which are about 75% and 73% of $\langle Cl\rangle_T$, respectively. The increment of the vortex lift coefficient is $\Delta\langle Cl_{vor}\rangle_T = \langle Cl_{vor}\rangle_T - \langle Cl_{vor}\rangle_{T,ref} \approx 4.7$, which is about 78% of the total increment of the lift coefficient of $\Delta\langle Cl\rangle_T \approx 6$. It is clear that vortex lift contributes considerably to lift enhancement in the dynamically changing wingspan.

An interesting finding is that the vortex lift coefficient Cl_{vor} is positive in not only the downstroke but also the upstroke in both the cases, indicating that the LEVs can still contribute to lift generation even when they are detached from the wing in the upstroke. It is observed in figure 5 that the LEVs generated in the downstroke still stay on the inner portion of the upper surface in the initial stage of the upstroke in the dynamically changing wingspan case. Actually, this is a kind of vortex capture mechanism similar to that in the flapping flight of insects. This is further evidenced in figure 10 by the distributions of the vertical component of the Lamb vector ($(\boldsymbol{u} \times \boldsymbol{\omega})_z$) that directly contributes to the vortex lift on the upper surface at 0.2 T after the start of the upstroke. From the top-views in figure 10, it is found that the positive $(\boldsymbol{u} \times \boldsymbol{\omega})_z$ field associated with the LEVs in the dynamically changing wingspan case [panel (*a*)] is much greater in magnitude than that in the fixed wingspan case [panel (*b*)]. There are the thin layers with the negative $(\boldsymbol{u} \times \boldsymbol{\omega})_z$ near the wall that correspond to the newly generated near-wall shear layers in the upstroke. The distributions of $(\boldsymbol{u} \times \boldsymbol{\omega})_z$ at 60% semi-wingspan from the body [Panels (*c*) and (*d*)] show that the magnitude of the positive $(\boldsymbol{u} \times \boldsymbol{\omega})_z$ associated with the LEVs near the leading edge and trailing edge in the dynamically changing wingspan case is much larger than that in the fixed wingspan case. In particular, there is a distinct blob of the large positive $(\boldsymbol{u} \times \boldsymbol{\omega})_z$ directly on the upper surface near the trailing edge in the dynamically changing wingspan case, which contributes to the positive lift at this phase of the upstroke. This blob is associated with the shed LEV captured in the early stage of the upstroke, which provides an explanation for the positive vortex lift in the upstroke. Figure 11 shows the distributions of the vertical component of the Lamb vector at 0.2 T after the start of the upstroke at the spanwise locations of 20, 40, 60 and 80% semi-wingspan. It is indicated that the larger vertical components of the Lamb vector are generated at these locations in the dynamically changing wingspan case.

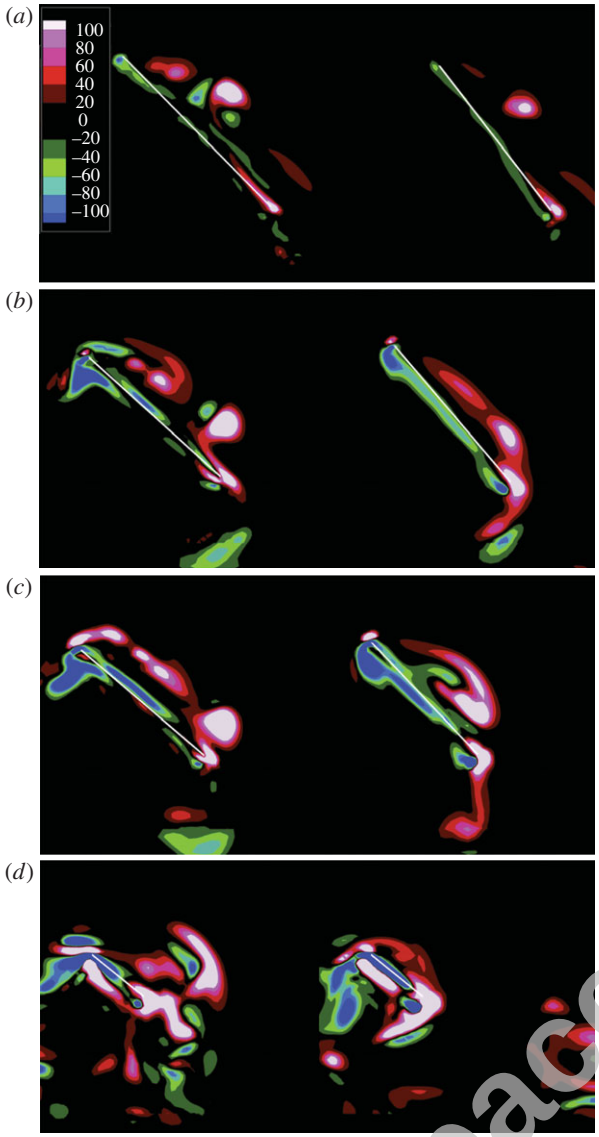

Figure 11. The distributions of the vertical component of the Lamb vector at 0.2 T after the start of upstroke at the spanwise locations of (*a*) 20, (*b*) 40, (*c*) 60 and (*d*) 80% semi-wingspan. The left column shows the dynamically changing wingspan case, and the right column shows the fixed wingspan case.

6. Efficiency of lift generation

For additional insight into the effect of dynamically changing wingspan, a non-dimensional parameter is defined as

$$\eta_L = \frac{\langle Cl \rangle_T}{\langle \hat{E} \rangle_T}, \tag{6.1}$$

where $\hat{E}$ is the non-dimensional mechanical energy consumed by the bat flapping wings in flight, $\langle Cl \rangle_T$ is the time-averaged lift coefficient, and $\langle \hat{E} \rangle_T$ is the time-averaged value of the non-dimensional mechanical energy consumed in flight. The parameter η_L describes the lift generation for a given amount of the mechanical energy consumed by the flapping wings in flight. Loosely speaking, η_L could be considered as the efficiency of lift generation if it is suitably normalized. The non-dimensional total kinetic energy of the fluid in a control volume V is defined as

$$\hat{E} = \frac{1}{2V} \sum_{i=1}^{N} \hat{u}_i^2 V_i, \tag{6.2}$$

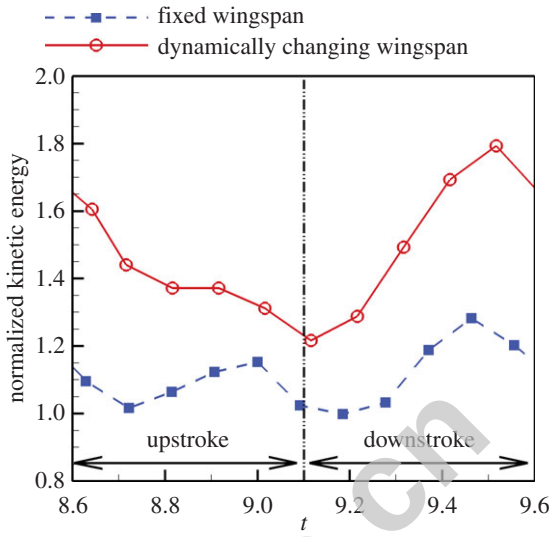

Figure 12. The time histories of the non-dimensional kinetic energy of the fluid in the dynamically changing wingspan case and the fixed wingspan case. (Online version in colour.)

where $\hat{u}_i^2 = u_i^2/U^2$ is the normalized fluid kinetic energy in the cell 'i', V_i is the volume of the cell 'i', N is the number of cells in the domain and U is the incoming flow (flight) velocity.

The time histories of the non-dimensional kinetic energy of the fluid are shown in figure 12 for the bat models with the dynamically changing wingspan case and the fixed wingspan case. The bat model with the dynamically changing wingspan generates more kinetic energy of the fluid than that with the fixed wingspan. The time-averaged values of the non-dimensional kinetic energy of the fluid in the dynamically changing wingspan case and the fixed wingspan case are $\langle \hat{E} \rangle_T = 1.5$ and $\langle \hat{E} \rangle_T = 1.1$, respectively. The parameter for the dynamically changing wingspan case is $\eta_L = 8.4$, compared to $\eta_L = 6$ for the fixed wingspan case. It is indicated that the bat model with the dynamically changing wingspan is more efficient in terms of generating lift for a given amount of the mechanical energy consumed in flight. It is because the dynamically changing wingspan of the bat wings enhances the strength of the LEVs, which contribute significantly to vortex lift.

7. Conclusion

The analysis based on DNS of the unsteady flow fields over a slow-flying bat reveals that the lift can be significantly enhanced by the dynamically changing wingspan of the bat wing. The evidence for this new observation is provided by carefully comparing the flow structures and lift generation between two bat models. The first bat model is reconstructed based on the measurement data of a slow-flying Pallas' long-tongued bat. The second bat model used as a reference has a fixed wingspan, while the streamwise and vertical kinematics remains the same as that of the first model. The flow structures and lift coefficients of the bat models are obtained in DNS by numerically solving the NS equations. It is found that the time-averaged lift coefficient in the first bat model with the dynamically changing wingspan is much larger than that in the reference model with the fixed wingspan.

The detailed flow structures obtained in DNS reveal that the dynamically changing wingspan significantly intensifies

the LEVs on the upper surface of a flapping bat wing in the downstroke. The generated LEVs stay near the upper surface in the early stage of the upstroke as a vortex capture mechanism. As a result, the lift is significantly enhanced by the dynamically changing wingspan. More quantitatively, after the lift is decomposed into the vortex lift and the fluid-acceleration term, it is found that the vortex lift associated with the LEVs is positive in both the downstroke and upstroke. The vortex lift is considerably increased due to the dynamically changing wingspan. Therefore, lift enhancement in bat flight is contributed to not only by the geometrical effect of changing the lifting-surface area but also by the fluid-mechanic effect of the altered vortical structures (particularly the LEVs) induced by the dynamically changing wingspan. The higher efficiency is also attained in terms of generating lift for a given amount of the mechanical energy consumed in flight.

Authors' contributions. G.H. and T.L. conceived the study and designed the research; S.W. developed the code and conducted the simulations; T.L. and S.W. drafted the manuscript; X.Z. designed the numerical algorithm. All authors contributed to the analysis and interpretation of data, the revisions of the manuscript and final approval for publication.

Competing interests. We declare we have no competing interests.

Funding. This work was supported by National Natural Science Foundation of China under project nos. 11302238, 11372331 and 11232011.

Acknowledgements. T.L. acknowledges the hospitality received at The State Key Laboratory of Nonlinear Mechanics during his visit where he accomplished this work.

References

1. Sun M. 2014 Insect flight dynamics: stability and control. *Rev. Mod. Phys*. **86**, 615–646. (doi:10.1103/RevModPhys.86.615)
2. Spedding GR, Hedenstrom A. 2009 PIV-based investigations of animal flight. *Exp. Fluids* **46**, 749–763. (doi:10.1007/s00348-008-0597-y)
3. Liu H. 2009 Integrated modeling of insect flight: from morphology, kinematics to aerodynamics. *J. Comput. Phys*. **228**, 439–459. (doi:10.1016/j.jcp.2008.09.020)
4. Wang ZJ. 2005 Dissecting insect flight. *Annu. Rev. Fluid. Mech*. **37**, 183–210. (doi:10.1146/annurev.fluid.36.050802.121940)
5. Sane SP. 2003 The aerodynamics of insect flight. *J. Exp. Biol*. **206**, 4191–4208. (doi:10.1242/jeb.00663)
6. Song J, Luo H, Hedrick TL. 2014 Three-dimensional flow and lift characteristics of a hovering ruby-throated hummingbird. *J. R. Soc. Interface* **11**, 20140541. (doi:10.1098/rsif.2014.0541)
7. Wan H, Dong H, Gai K. 2014 Computational investigation of cicada aerodynamics in forward flight. *J. R. Soc. Interface* **12**, 20141116. (doi:10.1098/rsif.2014.1116)
8. Liu T, Kuykendoll K, Rhew R, Jones S. 2006 Avian wing geometry and kinematics. *AIAA J*. **44**, 954–963. (doi:10.2514/1.16224)
9. Iriarte-Diaz J, Riskin DK, Breuer KS, Swartz SM. 2012 Kinematic plasticity during flight in fruit bats: individual variability in response to loading. *PLoS ONE* **7**, e36665. (doi:10.1371/journal.pone.0036665)
10. Kang C-K, Shyy W. 2013 Scaling law and enhancement of lift generation of an insect-size hovering flexible wing. *J. R. Soc. Interface* **10**, 20130361. (doi:10.1098/rsif.2013.0361)
11. Zheng ZC, Wei Z. 2012 Study of mechanisms and factors that influence the formation of vortical wake of a heaving airfoil. *Phys. Fluids* **24**, 103601. (doi:10.1063/1.4760258)
12. Norberg UM. 1981 Allometry of bat wings and legs and comparison with bird wings. *Phil. Trans. R. Soc.* **292**, 359–398. (doi:10.1098/rstb.1981.0034)
13. Swartz SM, Middleton KM. 2008 Biomechanics of the bat limb skeleton: scaling, material properties and mechanics. *Cells Tissues Organs* **187**, 59–84. (doi:10.1159/000109964)
14. Hedenstrom A, Johansson LC, Spedding GR. 2009 Bird or bat: comparing airframe design and flight performance. *Bioinspir. Biomim*. **4**, 015001. (doi:10.1088/1748-3182/4/1/015001)
15. Voigt CC, Winter Y. 1999 Energetic cost of hovering flight in nectar-feeding bats (Phyllostomidae: Glossophaginae) and its scaling in moths, birds and bats. *J. Comp. Physiol. B* **169**, 38–48. (doi:10.1007/s003600050191)
16. Stockwell EF. 2001 Morphology and flight maneuverability in new world leaf-nosed bats (Chiroptera: Phyllostomidae). *J. Zool*. **254**, 505–514. (doi:10.1017/S0952836901001005)
17. Muijres FT, Bowlin MS, Johansson LC, Hedenstrom A. 2012 Vortex wake, downwash distribution, aerodynamic performance and wing beat kinematics in slow-flying pied flycatchers. *J. R. Soc. Interface* **9**, 292–303. (doi:10.1098/rsif.2011.0238)
18. Muijres FT, Henningsson P, Stuiver M, Hedenström A. 2012 Aerodynamic flight performance in flap-gliding birds and bats. *J. Theor. Biol*. **306**, 120–128. (doi:10.1016/j.jtbi.2012.04.014)
19. Tian XD *et al*. 2006 Direct measurements of the kinematics and dynamics of bat flight. *Bioinspir. Biomim*. **1**, S10–S18. (doi:10.1088/1748-3182/1/4/S02)
20. Hubel TY, Hristov NI, Swartz SM, Breuer KS. 2009 Time-resolved wake structure and kinematics of bat flight. *Exp. Fluids* **46**, 933–943. (doi:10.1007/s00348-009-0624-7)
21. Hubel TY, Riskin DK, Swartz SM, Breuer KS. 2010 Wake structure and wing kinematics: the flight of the lesser dog-faced fruit bat, *Cynopterus brachyotis*. *J. Exp. Biol*. **213**, 3427–3440. (doi:10.1242/jeb.043257)
22. Riskin DK, Willis DJ, Iriarte-Diaz J, Hedrick TL, Kostandov M, Chen J, Laidlaw DH, Breuer KS, Swartz SM. 2008 Quantifying the complexity of bat wing kinematics. *J. Theor. Biol*. **254**, 604–615. (doi:10.1016/j.jtbi.2008.06.011)
23. Wolf M, Johansson LC, von Busse R, Winter Y, Hedenstrom A. 2010 Kinematics of flight and the relationship to the vortex wake of a Pallas' long tongued bat (*Glossophaga soricina*). *J. Exp. Biol*. **213**, 2142–2153. (doi:10.1242/jeb.029777)
24. Hedenstrom A, Johansson LC, Wolf M, von Busse R, Winter Y, Spedding GR. 2007 Bat flight generates complex aerodynamic tracks. *Science* **316**, 894–897. (doi:10.1126/science.1142281)
25. Muijres FT, Johansson LC, Barfield R, Wolf M, Spedding GR, Hedenstrom A. 2008 Leading-edge vortex improves lift in slow-flying bats. *Science* **319**, 1250–1253. (doi:10.1126/science.1153019)
26. Johansson LC, Wolf M, Hedenström A. 2009 A quantitative comparison of bird and bat wakes. *J. R. Soc. Interface* **7**, 61–66. (doi:10.1098/rsif.2008.0541)
27. Yu YL, Guan ZW. 2015 Learning from bat: aerodynamics of actively morphing wing. *Theor. Appl. Mech. Lett*. **5**, 13–15. (doi:10.1016/j.taml.2015.01.009)
28. Viswanath K, Nagendra K, Cotter J, Frauenthal M, Tafti DK. 2014 Straight-line climbing flight aerodynamics of a fruit bat. *Phys. Fluids* **26**, 021901. (doi:10.1063/1.4864297)
29. Anderson J, Anderson JD. 2010 *Fundamentals of aerodynamics*, 5th edn. New York, NY: McGraw-Hill.
30. Harbig R, Sheridan J, Thompson M. 2014 The role of advance ratio and aspect ratio in determining leading-edge vortex stability for flapping flight. *J. Fluid Mech*. **751**, 71–105. (doi:10.1017/jfm.2014.262)
31. Fu J, Hefler C, Qiu H, Shyy W. 2014 Effects of aspect ratio on flapping wing aerodynamics in animal flight. *Acta. Mech. Sinica* **30**, 776–786. (doi:10.1007/s10409-014-0120-z)
32. Deng J, Caulfield CP, Shao X. 2014 Effect of aspect ratio on the energy extraction efficiency of three-dimensional flapping foils. *Phys. Fluids* **26**, 043102. (doi:10.1063/1.4872224)
33. Wang S, Zhang X. 2011 An immersed boundary method based on discrete stream function formulation for two- and three-dimensional incompressible flows. *J. Comput. Phys*. **230**, 3479–3499. (doi:10.1016/j.jcp.2011.01.045)
34. Yang X, Zhang X, Li Z, He G-W. 2009 A smoothing technique for discrete delta functions with

application to immersed boundary method in moving boundary simulations. *J. Comput. Phys*. **228**, 7821–7836. (doi:10.1016/j.jcp.2009.07.023)

35. Wang S, He G, Zhang X. 2013 Parallel computing strategy for a flow solver based on immersed boundary method and discrete stream-function formulation. *Comput. Fluids* **88**, 210–224. (doi:10.1016/j.compfluid.2013.09.001)
36. Wang S, Zhang X, He G, Liu T. 2013 A lift formula applied to low-Reynolds-number unsteady flows. *Phys. Fluids* **25**, 093605. (doi:10.1063/1.4821520)
37. Wang J. 2000 Two dimensional mechanism for insect hovering. *Phys. Rev. Lett*. **85**, 2216–2219. (doi:10.1103/PhysRevLett.85.2216)
38. Buchholz JH, Smits AJ. 2005 On the evolution of the wake structure produced by a low-aspect-ratio pitching panel. *J. Fluid Mech*. **564**, 433–443. (doi:10.1017/S0022112005006865)
39. Buchholz JHJ, Smits AJ. 2008 The wake structure and thrust performance of a rigid low-aspect-ratio pitching panel. *J. Fluid Mech*. **603**, 331–365.
40. Dong H, Mittal R, Najjar FM. 2006 Wake topology and hydrodynamic performance of low-aspect-ratio flapping foils. *J. Fluid Mech*. **566**, 309–343. (doi:10.1017/S002211200600190X)
41. Jeong J, Hussain F. 1995 On the identification of a vortex. *J. Fluid Mech*. **285**, 69–94. (doi:10.1017/S0022112095000462)
42. Wang S, Zhang X, He G, Liu T. 2014 Lift enhancement by dynamically changing wingspan in forward flapping flight. *Phys. Fluids* **26**, 061903. (doi:10.1063/1.4884130)
43. Wang S, Zhang X, He G, Liu T. 2015 Numerical simulation of unsteady flows over a slow-flying bat. *Theor. Appl. Mech. Lett*. **5**, 5–8. (doi:10.1016/j.taml.2015.01.006)
44. Lentink D, Dickinson MH. 2009 Rotational accelerations stabilize leading edge vortices on revolving fly wings. *J. Exp. Biol*. **212**, 2705–2719. (doi:10.1242/jeb.022269)
45. Lentink D, Dickinson MH. 2009 Biofluiddynamic scaling of flapping, spinning and translating fins and wings. *J. Exp. Biol*. **212**, 2691–2704. (doi:10.1242/jeb.022251)
46. De Veubeke BF. 1976 The dynamics of flexible bodies. *Int. J. Eng. Sci*. **14**, 895–913. (doi:10.1016/0020-7225(76)90102-6)
47. Watts P, Mitchell EJ, Swartz SM. 2001 A computational model for estimating the mechanics of horizontal flapping flight in bats: model description and validation. *J. Exp. Biol*. **204**, 2873–2898.
48. Liu T, Wang S, Zhang X, He G. 2015 Unsteady thin airfoil theory revisited: application of a simple lift formula. *AIAA J*. **53**, 1493–1502.